Filling box flows in porous media

Chunendra K. Sahu†, and M. R. Flynn

Department of Mechanical Engineering, University of Alberta

Edmonton, AB, T6G 2G8, Canada

(Received ?; revised ?; accepted ?. - To be entered by editorial office)

We report upon a theoretical and experimental investigation of a porous medium "filling box" flow by specifically examining the details of the laminar, descending plume and its outflow in a control volume having an impermeable bottom boundary and sidewalls. The plume outflow is initially comprised of a pair of oppositely-directed gravity currents. The gravity currents propagate horizontally until they reach the lateral sidewalls at $y = \pm L$. The flow then becomes of filling box type, with a vertically ascending "first front" separating discharged plume fluid below from ambient fluid above. The flow details are described analytically by first deriving a new similarity solution for Darcy plumes with $\mathrm{Pe} > \mathcal{O}(1)$ where Pe is the Péclet number. From the similarity solution so obtained we then derive expressions for the plume volume flux and mean reduced gravity as functions of the vertical distance from the source. Regarding the plume outflow, a similarity solution adopted from Huppert & Woods (*J. Fluid Mech.*, vol. 292, 55–69, 1995) describes the height and front speed of the gravity currents, whereas a semi-implicit finite difference scheme is used to predict the first front elevation versus time and horizontal distance. As with high-Reynolds number filling box flows, that studied here is an example of a coupled problem: the gravity current source conditions are prescribed by the plume volume flux and mean reduced gravity. Conversely, discharged plume fluid may be re-entrained into the plume, be it soon or long after reaching the bottom impermeable boundary.

† Email address for correspondence: chunendra@ualberta.ca

To corroborate our model predictions, analogue laboratory experiments are performed with fresh water and salt water as the working fluids. Our experiments consider as independent variables the porous medium bead diameter and the plume source volume flux and reduced gravity. Predictions for the gravity current front position and height compare favourably against analogue measured data. Good agreement is likewise noted when considering either the mean elevation or the profile of the first front.

Results from this study may be adopted in modelling geological plumes. For example, our equations can be used to predict the time required for discharged plume fluid to return to the point of injection in the case of aquifers closed on the sides and below by impermeable boundaries.

Key words: Buoyancy-driven flow, filling box model, laminar plumes, first front, porous medium, gravity current.

---

1. Introduction

The behaviour of free plumes has been well studied since the development of the MTT equations (Morton *et al.* 1956). These describe the dynamics of a turbulent plume in an infinite stratified or unstratified ambient, and require the application of an empirically-determined entrainment coefficient to prescribe lateral inflow by turbulent engulfment. By adopting the MTT equations, the behaviour of a free plume in a closed control volume was studied by Baines & Turner (1969). The associated "filling box" model has fluid from the (descending) plume spreading laterally upon reaching the bottom of the control volume then forming an ever deepening layer. The top surface of this layer is referred to as the "first front"; it approaches the plume source asymptotically for large

time, t, so that $h_f \propto t^{2/3}$, where h_f is the first front elevation. The inner solution of the filling box flow describes the vertical variation of the plume volume, momentum and buoyancy fluxes. Conversely the outer solution predicts, among other quantities, the first front advection speed. In Baines & Turner's treatment, the horizontal motion of the discharged plume fluid was omitted, however, this flow was included in the form of a gravity current by later researchers e.g. Britter (1979), Manins (1979) and Kaye & Hunt (2007).

Whereas a voluminous literature has accumulated on the above convection problem and its application to mixing in chemical storage tanks (Germeles 1975), the built environment (Caulfield & Woods 2002; Nabi & Flynn 2013) and ocean basins (Manins 1979; Hughes & Griffiths 2006), comparatively less work has been conducted to understand plumes and filling box flows in porous media. However, this latter problem is very much deserving of attention because, here again, numerous industrial and environmental applications arise. For instance: (i) geological sequestration of supercritical CO_2 (sc-CO_2) into deep saline aquifers for purposes of isolating anthropogenic CO_2 (Baines & Worden 2004; Bickle *et al.* 2007). When brine becomes saturated with dissolved sc-CO_2 in the upper layer of aquifers, its density becomes larger than the unsaturated brine. There follows the appearance of negatively-buoyant plumes that result in convective dissolution of this dense sc-CO_2-brine mixture into the unsaturated brine below (Ennis-King & Paterson 2003). Thus in evaluating the long-term efficacy of carbon sequestration, convective dissolution of the injected sc-CO_2 into brine must be considered and this, in turn, requires an understanding of porous media plumes and their mixing with ambient fluid (Neufeld *et al.* 2010; MacMinn *et al.* 2012). Moreover, because of the finite horizontal and vertical extent of aquifers, such plumes must be often studied in the context of filling-box-type flows. (ii) dissolution of non-aqueous phase liquids (NAPL) in the subsurface

environment (Khachikian & Harmon 2000; Kueper *et al.* 2003). NAPL seepage through the vadose zone and into zones containing groundwater is primarily driven by density differences between the NAPL and groundwater. Because the zones in question may have restricted boundaries, filling box models should again be deployed in quantifying rates of mixing and contamination. Seeking to address some of the flow behaviours specific to these applications, the recent study of Roes *et al.* (2014) considered a filling box flow in a "leaky" porous medium, i.e. one having one or more discrete fissures, which allow for an outflow of discharged plume fluid. Steady state is achieved once this outflow equals the plume volume flux at the level of the (flat, stationary) first front. Note, however, that Roes *et al.* (2014) did not examine the transient approach towards steady state nor the case of a reservoir sealed by caprock boundaries devoid of fissures for which no steady state solutions exist. Further aspects of Roes et al.'s study are considered below.

Flows in porous media can be divided into the two following categories depending on the value of the Reynolds number, $\mathrm{Re} = \dfrac{d_0 U}{\nu}$, where d_0 is the mean grain diameter, U is a characteristic velocity that depends upon transport velocity, which we will define in section 2.1, and ν is the kinematic viscosity: (i) Darcy flow where $\mathrm{Re} \lesssim \mathcal{O}(10)$, and (ii) non-Darcy flow where $\mathrm{Re} > \mathcal{O}(10)$ (Bear 1972; Dullien 1992). A second, equally important non-dimensional number in (variable-component, miscible) porous media flow, is the Péclet number, $\mathrm{Pe} = \dfrac{d_0 U \tau}{D_d}$, in which D_d is the molecular diffusion coefficient and $\tau\,(> 1)$ is the tortuosity constant, which is defined as the ratio of the actual path length traveled by a solute molecule to the distance it would travel in the absence of a porous medium. The Péclet number characterizes the importance of advection vs. diffusion with diffusive transport playing a subordinate role to mechanical dispersive transport when $\mathrm{Pe} \gg \mathcal{O}(1)$. The combined influence of diffusion and dispersion can be modelled by

defining the following transport coefficient:

$$D = d_0 U \left(1 + \frac{1}{\mathrm{Pe}}\right) \tag{1.1}$$

(Delgado 2007; Houseworth 1984). When $\mathrm{Pe} \ll \mathcal{O}(1)$, $D \simeq \dfrac{D_d}{\tau}$, however, when $\mathrm{Pe} \gg \mathcal{O}(1)$, $D \simeq d_0 U$. In this latter limit, it is appropriate to refer to D as the dispersion coefficient.

The dynamics of rectilinear line plumes in porous media were first studied by Wooding (1963) for Darcy flow with $\mathrm{Pe} \ll \mathcal{O}(1)$. Starting from mass continuity, Darcy's law and a solute transport equation, Wooding (1963) derived a similarity solution based on the assumption that the plume is long and thin. On this basis, he obtained the following equation for the variation of the plume volume flux, Q, with the vertical coordinate, x:

$$Q = \left(\frac{36 D \phi F_0 k \Lambda^2 x}{\nu}\right)^{1/3}. \tag{1.2}$$

Here ϕ is the porosity, F_0 is the source buoyancy flux, k is the permeability and Λ is the source width in the third dimension.

Roes *et al.* (2014) adopted Wooding's equations into the $\mathrm{Pe} \gg \mathcal{O}(1)$ filling box framework, but could only do so by making a limiting assumption on D, namely that its numerical value was the same everywhere inside the porous medium. Although there exists some practical justification for this approach, this assumption is, strictly speaking incorrect: D depends upon the flow speed and the flow speed, in turn, varies both horizontally and vertically. In fact, Lai (1991) considered the case of spatially-variable D. However, Lai's analysis was complicated by the fact that, as with the earlier investigation by Chen & Ho (1986), he assumed a non-Darcy flow regime. Thus the Darcy equations were replaced by the Darcy-Forchheimer equations, which are obtained by introducing Dupuit-Forchheimer inertial terms into the Darcy equations (Nield & Kuznetsov 2013). These inertial terms are proportional to the square of the transport velocity and also

include a drag coefficient whose value depends on the geometry of the porous media. In these studies of non-Darcy plumes, it was proved that no similarity solution exists, and hence solutions were instead presented in terms of a non-similar variable, whose magnitude depended on various physical parameters e.g. the permeability and fluid viscosity.

Here we synthesize these previous approaches by assuming Darcy flow with a spatially-variable D. Our objectives are two-fold: (i) to derive self-similar plume equations in a rectilinear geometry germane to this case and, (ii) to use the associated solutions to examine the time-dependent behaviour of porous media filling box flows, from which various pertinent flow time-scales can be estimated. Importantly, our analysis includes a description of the gravity current dynamics associated with plume outflow along the impermeable bottom boundary. As noted above, these dynamics are sometimes omitted when studying turbulent free plumes. The theory is validated (where possible) by comparison with analogue laboratory experiments that employ salt water and fresh water, respectively, as the source and ambient fluids.

The rest of the manuscript is organized as follows. Our plume solution is given in section 2.1 whereas sections 2.2 and 2.3 describe, respectively, the gravity current and the ascending first front. Thereafter in section 3, the laboratory experiments are discussed. This description is followed by a comparison between theory and experiment which appears in section 4. Finally section 5 presents conclusions of this work and identifies topics for future study.

2. Theory

2.1. *Plume in an unbounded medium*

To derive a solution for laminar plume flow in a porous medium, we begin by presenting the governing equations based on mass and momentum continuity, solute transport and

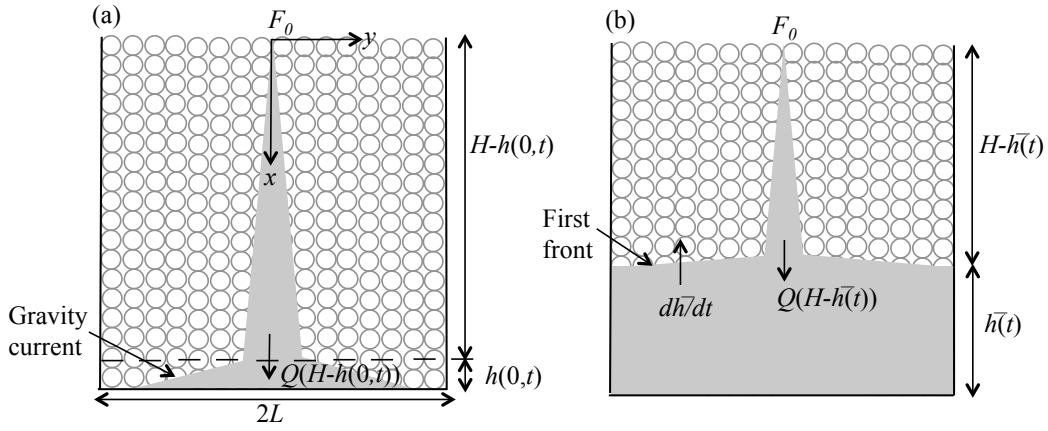

Figure 1: Convection in a confined porous medium: (a) plume and gravity current flow, (b) advection of the first front towards the source.

a linear equation of state. In contrast to Wooding (1963) and Roes *et al.* (2014), we consider a dispersion coefficient that varies in x and y, where the x and y directions are defined in figure 1.

The flow is assumed to be steady, Boussinesq and two dimensional-rectilinear and the ambient is assumed to remain unstratified above the first front so that the governing equations read

$$\frac{\partial u}{\partial x} + \frac{\partial v}{\partial y} = 0 \qquad \text{[mass continuity]}, \tag{2.1}$$

$$\frac{1}{\rho_0}\frac{\partial P}{\partial x} + \frac{\nu}{k}u = \frac{g\rho}{\rho_0} \qquad \text{[momentum cont. in } x\text{]}, \tag{2.2}$$

$$\frac{1}{\rho_0}\frac{\partial P}{\partial y} + \frac{\nu}{k}v = 0 \qquad \text{[momentum cont. in } y\text{]}, \tag{2.3}$$

$$\frac{1}{\phi}\left(u\frac{\partial C}{\partial x} + v\frac{\partial C}{\partial y}\right) = \frac{\partial}{\partial x}\left(D_{\mathrm{L}}\frac{\partial C}{\partial x}\right) + \frac{\partial}{\partial y}\left(D_{\mathrm{T}}\frac{\partial C}{\partial y}\right) \qquad \text{[solute transport]}, \tag{2.4}$$

$$\rho = \rho_0(1 + \beta C) \qquad \text{[linear equation of state]}. \tag{2.5}$$

Here P is the fluid pressure, C is the solute concentration and β is the solute contraction coefficient. Moreover, ρ is the fluid density, whose far-field value is ρ_0 corresponding to a

solute concentration of zero. Furthermore, D_{L} and D_{T} are the longitudinal and transverse dispersion coefficients.

The momentum equations, (2.2) and (2.3), are combined to eliminate the fluid pressure, whereby

$$\frac{\nu}{k}\left(\frac{\partial u}{\partial y}-\frac{\partial v}{\partial x}\right)=\frac{g}{\rho_0}\frac{\partial \rho}{\partial y}. \tag{2.6}$$

We then apply Wooding's boundary layer approximation so that

$$\left|\frac{\partial v}{\partial x}\right| \ll \left|\frac{\partial u}{\partial y}\right|, \quad \text{and} \quad \left|\frac{\partial}{\partial x}\left(D_{\mathrm{L}}\frac{\partial C}{\partial x}\right)\right| \ll \left|\frac{\partial}{\partial y}\left(D_{\mathrm{T}}\frac{\partial C}{\partial y}\right)\right|. \tag{2.7}$$

The validity of the latter boundary layer approximation is outlined at the end of section 2.1.

Following Delgado (2007), Houseworth (1984) and others, for $\mathrm{Pe} \gg \mathcal{O}(1)$, the transverse dispersion coefficient can be expressed as

$$D_{\mathrm{T}} \simeq \alpha u. \tag{2.8}$$

Here α is the transverse dispersivity, and its value shall, consistent with the turbulent plume entrainment coefficient (Morton *et al.* 1956), be determined based on experimental measurement. The above representation for D_{T}, in particular the use of u rather than the horizontal transport velocity, v, and the incorporation of α follows from the methodology of Lai (1991). Finally, and for $\mathrm{Pe} \gg \mathcal{O}(1)$, we can now make a connection between u and the characteristic velocity, U, that appears in (1.1), i.e $U = \dfrac{\alpha u}{d_0}$.

On the basis of the above discussion, (2.4) becomes

$$u\frac{\partial C}{\partial x}+v\frac{\partial C}{\partial y}=\alpha\phi\frac{\partial}{\partial y}\left(u\frac{\partial C}{\partial y}\right). \tag{2.9}$$

Furthermore, a stream-function, ψ, is introduced such that $u = \dfrac{\partial \psi}{\partial y}$ and $v = -\dfrac{\partial \psi}{\partial x}$. Equations (2.6) and (2.9) can then be rewritten as

$$\frac{\partial^2 \psi}{\partial y^2}=\frac{g\beta k}{\nu}\frac{\partial C}{\partial y} \tag{2.10}$$

$$\frac{\partial\psi}{\partial y}\frac{\partial C}{\partial x}-\frac{\partial\psi}{\partial x}\frac{\partial C}{\partial y}=\alpha\phi\left(\frac{\partial^2\psi}{\partial y^2}\frac{\partial C}{\partial y}+\frac{\partial\psi}{\partial y}\frac{\partial^2 C}{\partial y^2}\right), \tag{2.11}$$

respectively. We seek a self-similar solution to (2.10) and (2.11) of the form

$$\psi=A_1x^p\mathcal{F}(\eta),\quad C=A_2x^q\mathcal{G}(\eta) \tag{2.12}$$

where the self-similar variable, η, is defined as $\eta=A_3\dfrac{y}{x^n}$. The constants, $p,\ q,\ n,\ A_1,\ A_2$ and A_3, will be determined shortly. Applying (2.12) in (2.10) yields

$$A_1x^p\mathcal{F}''\left(\frac{A_3}{x^n}\right)^2=\frac{g\beta k}{\nu}A_2x^q\mathcal{G}'\frac{A_3}{x^n}. \tag{2.13}$$

Thus, $\mathcal{G}(\eta)=\mathcal{F}'(\eta)\equiv\mathrm{d}\mathcal{F}/\mathrm{d}\eta$, $n=p-q$ and $A_2=A_1A_3\dfrac{\nu}{g\beta k}$. Hence, (2.11) becomes

$$x^{2q-1}\{[q\mathcal{F}'-(p-q)\mathcal{F}''\eta]\mathcal{F}'-[p\mathcal{F}-(p-q)\mathcal{F}'\eta]\mathcal{F}''\}=\alpha\phi A_3^2x^{2(2q-p)}\left(\mathcal{F}''\mathcal{F}''+\mathcal{F}'''\mathcal{F}'\right). \tag{2.14}$$

The factors of x that appear on the left- and right-hand sides of the equation disappear provided $p-q=\dfrac{1}{2}$. Equation (2.14) is further simplified by selecting $A_3=\dfrac{1}{\sqrt{\alpha\phi}}$ whereupon

$$\mathcal{F}'''\mathcal{F}'+\mathcal{F}''\mathcal{F}''+p\mathcal{F}''\mathcal{F}-q\mathcal{F}'\mathcal{F}'=0. \tag{2.15}$$

To determine the values for p and q, we recall that the buoyancy flux, F_0, is conserved i.e. it is independent of the vertical coordinate in an unstratified medium. Formally, F_0 is defined as

$$F_0=\Lambda\int_{-\infty}^{\infty}ug'\,\mathrm{d}y,$$

where $g'=g\dfrac{\rho-\rho_0}{\rho_0}\equiv g\beta C$ is the reduced gravity. By applying the above results, it can be shown that

$$F_0=\Lambda g\beta A_1A_2x^{(p+q)}\int_{-\infty}^{\infty}\mathcal{F}'^2\,\mathrm{d}\eta, \tag{2.16}$$

which implies that $p+q=0$. But we previously showed that $p-q=\frac{1}{2}$ and therefore

$p = \frac{1}{4}$ and $q = -\frac{1}{4}$. Consequently, (2.15) takes the form

$$\mathcal{F}'''\mathcal{F}' + \mathcal{F}''\mathcal{F}'' + \frac{1}{4}\mathcal{F}''\mathcal{F} + \frac{1}{4}\mathcal{F}'\mathcal{F}' = (\mathcal{F}''\mathcal{F}')' + \frac{1}{4}(\mathcal{F}'\mathcal{F})' = 0. \tag{2.17}$$

In solving (2.17), we recall the assumption that $D \simeq d_0\bar{U}$ i.e. Pe $\gg \mathcal{O}(1)$. In the neighbourhood of the plume center-line, this is a reasonable approximation, however, its validity is highly suspect far away from the center-line where flow velocities become small. We therefore restrict ourselves to finding an "inner" solution to (2.15), valid in the limit of small y (small η). In the outer region, by contrast, spatial variations in u, v or S are ignored. Such a division of the flow into inner and outer regions would be inappropriate in case of constant D (Wooding 1963; Roes *et al.* 2014), but is, in fact, not at all dissimilar to the approach followed in the "top hat" description of free turbulent plumes where molecular diffusive effects are likewise ignored (Morton *et al.* 1956; Linden *et al.* 1990). We therefore proceed by integrating (2.17) remembering that $\mathcal{F}'(\eta) = \mathcal{G}(\eta)$ prescribes the non-dimensional solute concentration. This concentration cannot be negative and must vanish altogether in the far field; symbolically, $C(x, y) > 0 \Rightarrow \mathcal{F}'(\eta) > 0$ and $C(x, \pm\infty) = C_0 \Rightarrow \mathcal{F}'(\pm\infty) = 0$. Symmetric suggests, moreover, that the concentration must be identical left and right so that $C(x, y) = C(x, -y) \Rightarrow \mathcal{F}'(\eta) = \mathcal{F}'(-\eta)$. Symmetry also requires that $\psi(x, 0) = 0$ so that $\mathcal{F}(0) = 0$. Therefore it can be shown that

$$\mathcal{F} = \begin{cases} -c, & \eta < -\pi \\ c\sin\dfrac{\eta}{2}, & -\pi < \eta < \pi \\ c, & \eta > \pi \end{cases} \quad \text{and} \quad \mathcal{G} = \mathcal{F}' = \begin{cases} \dfrac{c}{2}\cos\dfrac{\eta}{2}, & -\pi < \eta < \pi \\ 0, & |\eta| > \pi \end{cases}. \tag{2.18}$$

Here c is a constant of integration and will automatically disappear shortly. Note that (2.18) is the only symmetric, nontrivial solution to (2.17) satisfying $\mathcal{G} = \mathcal{F}' \geqslant 0$. Now on

applying (2.16), and recalling that $A_2 = A_1 A_3 \dfrac{\nu}{g\beta k}$, we find

$$A_1 = \left(\frac{F_0 k}{\Lambda \nu} \frac{\sqrt{\alpha d_0 \phi}}{\int_{-\infty}^{\infty} \mathcal{F}'^2 \, d\eta} \right)^{1/2}.$$

Equation (2.18) can then be combined with (2.12) to determine the volume flux, Q, of the plume. More specifically,

$$Q = \Lambda \int_{-\infty}^{\infty} u \, \mathrm{d}y = \left[\left(\frac{16 F_0 k \Lambda}{\pi \nu} \right)^2 \phi \alpha x \right]^{1/4}. \tag{2.19}$$

Similarly, the plume momentum flux and mean reduced gravity are found to be, respectively,

$$M = \frac{F_0 k}{\nu} \quad \text{and} \quad \bar{g}' = \frac{F_0}{Q} = \left[\left(\frac{\pi F_0 \nu}{16 k \Lambda} \right)^2 \frac{1}{\phi \alpha x} \right]^{1/4}. \tag{2.20}$$

Note that Q and $\bar{g}'$ are proportional to $x^{1/4}$ and $x^{-1/4}$, respectively, whereas in previous investigations such as Wooding (1963) and Roes *et al.* (2014) where $\mathrm{Pe} \lesssim \mathcal{O}(1)$, these quantities are proportional to $x^{1/3}$ and $x^{-1/3}$. The formula for M is unchanged, however, because our plumes plus those of Wooding (1963) satisfy the conditions for Darcy flow.

Equation (2.19) is derived in the limit of an ideal plume whereby $Q \to 0$ as $x \to 0$. However, for a nonideal plume, which has a finite source volume flux, this assumption cannot be applied. Therefore, a virtual origin correction is determined by extrapolating the flow to negative x-values and a fictitious point, $x = -x_0$, where the plume volume flux vanishes (Wooding 1963; see also Hunt & Kaye 2001). More formally, x_0 is given by

$$x_0 = \frac{1}{\phi \alpha} \left(\frac{\pi \nu}{16 F_0 k \Lambda} \right)^2 {Q_0}^4 \tag{2.21}$$

so that the plume volume flux and mean reduced gravity are given, respectively, by

$$Q = \left[\left(\frac{16 F_0 k \Lambda}{\pi \nu} \right)^2 \phi \alpha (x + x_0) \right]^{1/4} \tag{2.22}$$

and

$$\bar{g}' = g \beta \bar{C} = \left[\left(\frac{\pi F_0 \nu}{16 k \Lambda} \right)^2 \frac{1}{\phi \alpha (x + x_0)} \right]^{1/4}. \tag{2.23}$$

We prefer to think of solute concentration in terms of its influence on buoyancy, thus our preference for using $\bar{g}'$ in place of $\bar{C}$. But the relationship between the two is, by virtue of the linear equation of state (2.5), very direct, as confirmed by the above equation.

Finally, we verify the validity of the boundary layer approximation made in (2.7) by estimating, using scaling analysis, the range of $D_{\rm L}$ and $D_{\rm T}$ for which the stated inequality holds. When (2.7) is valid,

$$\frac{D_{\rm L}C}{L_x^2} \ll \frac{D_{\rm T}C}{L_y^2} \quad \text{or} \quad \frac{D_{\rm L}}{D_{\rm T}} \ll \left(\frac{L_x}{L_y}\right)^2 \tag{2.24}$$

where L_x and L_y respectively denote characteristic vertical and horizontal length scales associated with the plume. Given the finite size of the control volume shown schematically in figure 1, we choose $L_x = H$. Conversely, L_y is defined to be the plume width at $x = H$; following from the self-similar solution obtained in (2.18), it can be shown that $L_y \sim \pi\sqrt{\alpha H}$. Thus (2.24) holds provided

$$\frac{D_{\rm L}}{D_{\rm T}} \ll \frac{H}{\pi^2\alpha}. \tag{2.25}$$

Using results from section 4, it can be argued that $\dfrac{1}{\pi^2\alpha} \sim \mathcal{O}(0.1)\,\mathrm{cm}^{-1}$, at least for the experiments of interest here. Moreover, $H \sim \mathcal{O}(10)\,\mathrm{cm}$ and therefore, in the present context, $\dfrac{H}{\pi^2\alpha} \sim \mathcal{O}(10^2)$. By contrast, we expect $\dfrac{D_{\rm L}}{D_{\rm T}}$ to be significantly less: according to Bear & Verruijt (1987), $\dfrac{D_{\rm L}}{D_{\rm T}} \simeq 100$ only for large Péclet numbers, i.e. $\mathrm{Pe} \sim \mathcal{O}(10^6)$, roughly three orders of magnitude greater than the values of Pe relevant to our laboratory experiments. We therefore expect (2.25) to be satisfied both experimentally and, equally importantly, in real geophysical flows for which H and α are expected to be larger and smaller, respectively, than the values germane to section 3.

2.2. *Gravity current*

When the plume fluid collides with the (impermeable) bottom boundary of the control volume a pair of gravity currents, traveling in the $+y$ and $-y$ directions, are formed

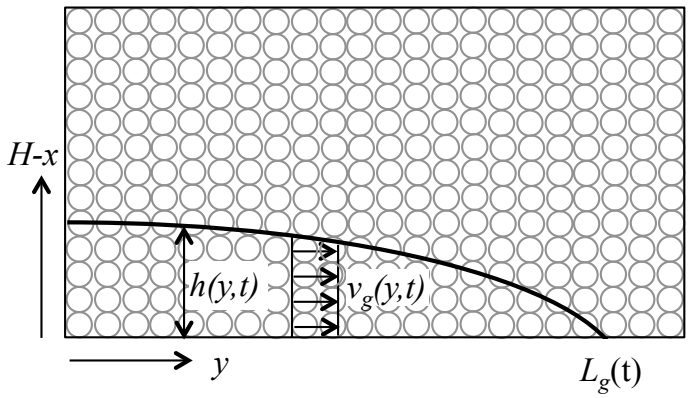

Figure 2: Gravity current flow in a porous medium.

(Manins 1979; Kaye & Hunt 2007). Although the flow initiates at the instant that the source nozzle is "switched on", we take $t = 0$ to be the time when plume fluid first reaches the bottom boundary. We justify this assumption as follows. Using (2.12) and (2.18), it is straightforward to estimate the time, t_R, that a fluid particle resides within the plume whilst flowing a vertical distance H. (The residence time associated with flow within a thermal is expected to be larger than, but still comparable to, the residence time associated with flow within a plume.) Comparing t_R against the time, t_L, required for the gravity current to reach the lateral sidewalls, we find that $t_R/t_L \sim \mathcal{O}(10^{-1})$ for the geometry of interest here. (The time-scale t_L is defined more precisely below.) In like fashion, $t_R/t_H \sim \mathcal{O}(10^{-2})$ where t_H, defined in section 2.3, is the time required for the first front to reach the top of the control volume. By ignoring the flow dynamics within the time interval t_R, we implicitly exclude from considering control volumes that are tall and narrow. However, this case is not representative of many real geophysical scenarios where $L \gg H$ and, in any event, is unlikely to yield well-defined gravity currents of the type investigated below in section 2.2.

The propagation of a gravity current through a porous medium has been described by Huppert & Woods (1995) – only a brief review of their formulation is provided below.

Presuming a hydrostatic flow, the gravity current horizontal flow speed, v_g, is depth-independent and varies with $\partial h/\partial y$ where h is the interface height (see figure 2) according to

$$v_g = -\frac{kg'_g}{\nu}\frac{\partial h}{\partial y} \tag{2.26}$$

(Huppert & Woods 1995, equation 2.5). Here g'_g is the reduced gravity of the discharged plume fluid turned gravity current fluid. Strictly speaking, g'_g is a function of t, however, we verify below that the time rate of change of g'_g is small enough to be considered negligible, at least for the problem of interest here.

The equation of local volume flux balance reads

$$\phi\frac{\partial h}{\partial t} = -\frac{\partial}{\partial y}\left[\int_0^{h(y,t)} v_g(y,t)\,\mathrm{d}(H-x)\right]. \tag{2.27}$$

On substituting (2.26) into (2.27), it can easily be shown that

$$\frac{\partial h}{\partial t} - S\frac{\partial}{\partial y}\left(h\frac{\partial h}{\partial y}\right) = 0. \tag{2.28}$$

where $S = \dfrac{kg'_g}{\nu\phi}$. Also, the boundary condition at the leading edge of the gravity current and the mass conservation equation are given by

$$h(L_g(t),t) = 0 \quad \text{and} \quad \phi\int_0^{L_g(t)} h(y,t)\,\mathrm{d}y = V(t), \tag{2.29}$$

respectively (Huppert & Woods 1995, equation 3.5). Here V is the total volume of discharged plume fluid turned gravity current fluid measured from the initial instant, when the plume first reaches the bottom surface, up to time t at which point the gravity current is L_g units long.

The methodology presented by Huppert & Woods (1995) is adopted to solve (2.28);

thus, we seek a self-similar solution of the form

$$h = \left(\frac{Q_g^2}{S}t\right)^{1/3} \mathcal{H}(\xi) \quad \text{where} \quad \xi = \left(\frac{1}{Q_g S}\right)^{1/3} \frac{y}{t^{2/3}} \quad \text{and} \quad t \not\to 0. \tag{2.30}$$

Here Q_g is the volume flux per unit span of the discharged plume fluid turned gravity current fluid. With a similar argument as above for g'_g, we neglect the time dependence of Q_g for which a verification is presented at the end of this section. After some simplification, the PDE (2.28) can be rewritten as the following ODE in ξ:

$$3\mathcal{H}''\mathcal{H}' + 3\mathcal{H}'\mathcal{H}' + 2\xi\mathcal{H}' - \mathcal{H} = 0. \tag{2.31}$$

The associated boundary conditions, which come from (2.29), read

$$\mathcal{H}(\lambda) = 0 \quad \text{and} \quad \phi \int_0^\lambda \mathcal{H}\, d\xi = 1 \tag{2.32}$$

where λ is the dimensionless length of the gravity current so that $\max(\xi) = \lambda$. A numerical solution is obtained for (2.31) by employing a shooting method to find $\mathcal{H}(\xi = 0)$ and λ. Note that in this equation, ξ is the independent variable of integration, not t. Therefore, we initialize our solver using a "clever guess" for the appropriate condition at $\xi = 0$ and solve the ODE. We then look to see whether the volume conservation equation $\phi \int_0^\lambda \mathcal{H}\, d\xi = 1$ is satisfied given that $\mathcal{H}(\lambda) = 0$. The "clever guess" is then updated and the process repeated till the solution converges. Numerical values of $\mathcal{H}(\xi = 0)$ and λ are found to be, respectively, 2.470 and 2.046. The solution obtained is then used to predict the gravity current shape as a function of time for which sample results are exhibited in figure 3. Because $t = 0$ is outside of the region of interest here, the final solution is plotted only for $t \gg 0$.

It should be noted that the result obtained from the similarity solution is only valid when the gravity current is long and thin, i.e. $h(0, t) \ll L_g(t)$. Here $L_g(t)$ is the length

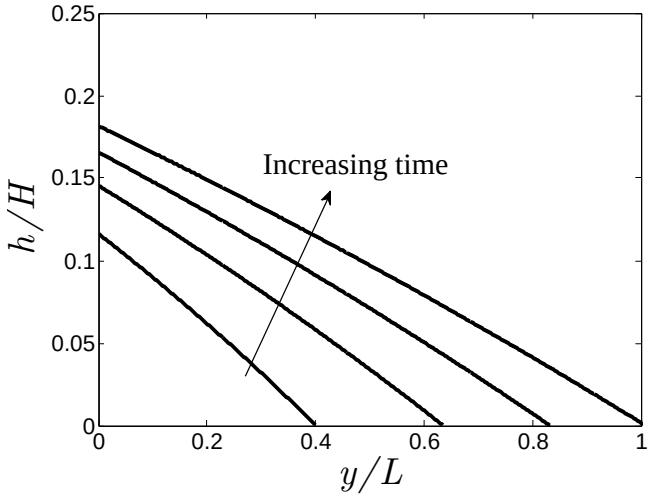

Figure 3: Gravity current height and length vs time. The non-dimensional time increment is $0.25t_L$, starting with $t = 0.25t_L$ for the lowest curve and finishing with $t = t_L$ with the gravity current front located at $y/L = 1$. Also, $S = \dfrac{kg'}{\phi\nu} = 0.6$ cm/s, where $\phi = 0.38$.

of the gravity current and is given as

$$L_g = \lambda (Q_g S)^{1/3} t^{2/3}. \tag{2.33}$$

Furthermore, the time required by the gravity current front to reach the sidewall of the control volume, which is at a horizontal distance L from the source, is

$$t_L = \left[\left(\frac{L}{\lambda} \right)^3 \frac{1}{Q_g S} \right]^{1/2}. \tag{2.34}$$

From (2.33) and (2.34), a straightforward relation between the dimensionless length and time can be derived as

$$\frac{L_g}{L} = \left(\frac{t}{t_L} \right)^{2/3}. \tag{2.35}$$

Note also that when $t = t_L$, the mean height of the gravity current is given by

$$\bar{h}_{t_L} = \frac{1}{L} \int_0^L h(y, t_L)\, \mathrm{d}y = \frac{1}{\lambda} \left(\frac{Q_g^2}{\phi^3 S} t_L \right)^{1/3}. \tag{2.36}$$

This mean height of the gravity current will be used in section 4 when comparing the theoretical model with the experimental measurements.

From (2.22) and (2.23) we observe that $Q_g \propto (1 - h/H)^{1/4}$ and $g'_g \propto (1 - h/H)^{-1/4}$, respectively. Furthermore, $h/H \ll 1$ – see figure 3. These observations support our assumption that the time rates of change of Q_g and g'_g are negligible. For instance, the change in Q_g and g'_g between the times, $t = 0.25t_L$ and $t = t_L$ for the curves presented in figure 3 are -1.59% and 1.59%, respectively, whereas the increase in time is 300%.

2.3. *First front*

After the gravity current reaches the sidewall of the control volume, the dense fluid near the sidewall begins to move primarily vertically. Following the terminology introduced by Baines & Turner (1969), we refer to the interface between the discharged plume fluid and the overlying ambient fluid as the first front. Whereas the first front evolves in time and becomes horizontal in the long-time limit, its initial profile is prescribed by the shape of the gravity current at $t = t_L$. For $t > t_L$, the pressure remains hydrostatic and therefore the horizontal velocity below the first front remains independent of x. Hence, (2.28) can be employed to describe the spatio-temporal evolution of the first front. In this case, however, one must replace the front condition (2.29a) with a no-flux condition at the (impermeable) sidewalls. Symbolically

$$\partial h/\partial y = 0 \quad \text{when} \quad y = \pm L \quad \text{and} \quad t > t_L. \tag{2.37}$$

The second boundary condition is obtained from a straightforward extension of (2.29b), i.e.

$$\phi \int_0^L [h(y, t - t_L) - h(y, t_L)] \, \mathrm{d}y = V(t - t_L). \tag{2.38}$$

The finite length of the box obviously imposes an external length-scale on the problem at hand and, as a consequence, no self-similar solution is possible. However, a numerical

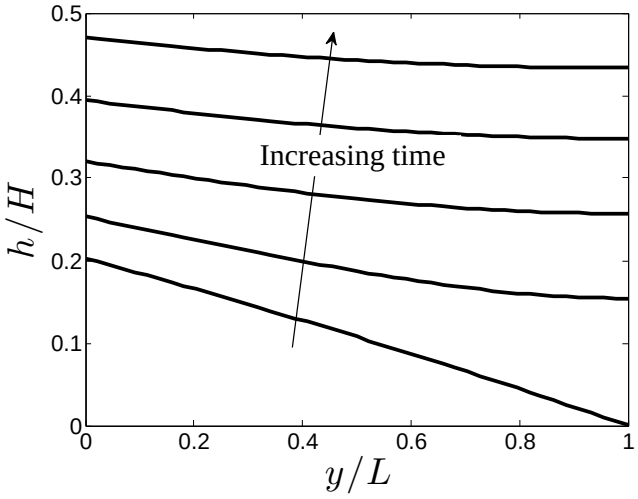

Figure 4: Evolution of the first front. The non-dimensional time increment is $0.08t_H$, starting with $t = t_L$ for the lowest curve. Note that t_H is defined by (2.43). The values used for the numerical scheme are: $\frac{\Delta y}{L} = 10^{-3}$, $\frac{\Delta t}{t_H} = 10^{-6}$ and $S = \frac{kg'}{\phi\nu} = 0.6$ cm/s, where $\phi = 0.38$.

solution can be obtained by applying a semi-implicit finite difference scheme (Causon & Mingham 2010). We rewrite (2.28) in the form

$$\frac{\partial h}{\partial t} = \frac{S}{2}\frac{\partial^2 h^2}{\partial y^2}. \tag{2.39}$$

The numerical solution is then obtained using the methodology outlined in Appendix A; sample results are given in figure 4.

As the first front advects upward, its curvature diminishes in time so that as $t \to \infty$, the boundary between discharged plume fluid and external ambient fluid becomes horizontal. The vertical advection of the first front can then be determined by simple volume flux balance, i.e.

$$\lim_{t\to\infty}[\phi A U_f(h)] = \lim_{t\to\infty}[Q(x = H - h)] \tag{2.40}$$

where Q is defined by (2.22), A is the control volume cross-sectional area, which is

assumed to be both constant and much larger than that of the plume, and U_f is the vertical velocity of the (horizontal) first front, which has an elevation of h, i.e. $U_f(h) = \dfrac{\mathrm{d}h}{\mathrm{d}t}$. Even before the long time limit is realized, (2.40) can still be applied provided h and U_f are replaced by their y-averaged mean values, i.e.

$$\phi A \bar{U}_f(\bar{h}) = Q(H - \bar{h}) \tag{2.41}$$

where $\bar{U}_f(h) = \dfrac{\mathrm{d}\bar{h}}{\mathrm{d}t}$. After applying (2.22), and with further integration and simplification, the predicted vertical distance, $\bar{h}_2 - \bar{h}_1$, traveled by the first front in time $t_2 - t_1$ can be determined from

$$\bar{h}_2 = H + x_0 - \left[(H + x_0 - \bar{h}_1)^{3/4} - \frac{3}{4} \frac{(t_2 - t_1)}{A} \left(\frac{16 F_0 k \Lambda \alpha^{1/2}}{\pi \nu \phi^{3/2}} \right)^{1/2} \right]^{4/3}. \tag{2.42}$$

By rearranging (2.42) and setting $\bar{h}_2 = H + x_0$ and $\bar{h}_1 = \bar{h}_{t_L}$, we obtain the following characteristic time-scale associated with the ascent of the first-front from the bottom to the top of the control volume:

$$t_H = \frac{4}{3} A \left(\frac{\pi \nu \phi^{3/2}}{16 F_0 k \Lambda \alpha^{1/2}} \right)^{1/2} (H + x_0 - \bar{h}_{t_L})^{3/4}. \tag{2.43}$$

Qualitatively, this result is similar to (B3) of Caulfield & Woods (2002), who studied filling box flows for a control volume devoid of porous material and containing a free turbulent plume.

3. Laboratory set-up and experiments

Laboratory experiments were performed to verify select theoretical predictions from section 2. A transparent acrylic rectangular box 88.9 cm long × 7.6 cm wide × 50.8 cm tall was filled with tap water and Potters Industries A Series Premium glass beads. The beads were of uniform size, and had a diameter of either 0.3 cm or 0.5 cm and a density of $1.54\,\mathrm{g/cm^3}$ as compared to $0.99\,\mathrm{g/cm^3}$ for the tap water. We assume a porosity of $\phi = 0.38$ for randomly distributed spherical beads (Happel & Brenner 1991).

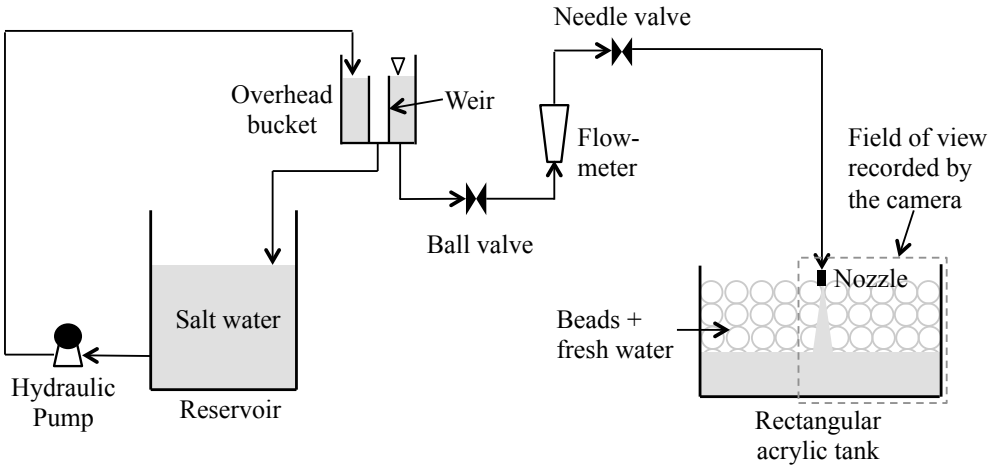

Figure 5: Schematic of the experimental set-up.

A schematic of the experimental set-up is shown in the figure 5. A specially designed line nozzle, manufactured to minimize the momentum of the source fluid by limiting the discharge velocity (Roes 2014, Appendix C.3), was used as the source and had a discharge area, $A_{\text{nozzle}} = 2.8$ cm^2. For simplicity, the nozzle, which spanned the width of the box, was positioned on-centre at $y = 0$. However, we expect that similar observations would have been recorded had the nozzle been located off-center (but not too close to either sidewall). An overhead bucket was used for supplying dense fluid, which consisted of salt water dyed with Procion MX Cold Water dye. Dye was used for flow visualization purposes; its addition did not change the fluid density ($<$1.10 g/cm^3) or kinematic viscosity (0.01 cm^2/s). The overhead bucket contained a cylindrical internal weir to maintain a constant level. A Gilmont GV-2119-S-P flowmeter was used to measure the (time-invariant) source volume flux which was set with the help of a ball valve and a needle valve. The overhead bucket was, in turn, supplied by a reservoir having a maximum capacity of 100 L. Fluid densities were measured to an accuracy of 0.00005 g/cm^3 using an Anton Paar DMA 4500 density meter.

A Canon Rebel EOS T2i 18.0 PM camera with an 18-55 mm IS II zoom lens was used to capture experimental images, which were collected every 120 s. Thus, over the course a single experiment, which usually took approximately 3 h to complete, roughly 90 images were recorded. The camera was placed perpendicular to the front face of the acrylic tank below which was located a mirror angled at 45° whose purpose was to provide details of the gravity current advance. The tank was backlit using a 3M 1880 overhead projector; to diffuse the light from this projector, a large sheet of white sketching paper was taped to the back of the tank. To minimize parallax effects, and also because of the symmetric nature of the flow, only one-half of the tank was in the field of view of the camera (figure 5).

All experimental images, including reference images which were recorded before the start of each experiment, were cropped to remove unwanted regions outside of the flow domain. Cropped images were then converted into gray-scale and the reference image was subtracted to specifically highlight the descending plume, gravity current and ascending first front. Subtracted images were then divided into 20 vertical bands of equal width with bands 3 through 20 falling outside of the near plume region. We used the post-processing algorithm described in Roes (2014) to estimate the interface height of the gravity current or first front in each of bands 3 through 20. Thus in each band and for every time instant, pixels were first binned into 10×10 boxes. Row-averaged pixel intensities were then calculated, which allowed us to compute the elevation corresponding to the maximum vertical intensity gradient. To improve upon this initial estimate for the interface height, data within $\pm$ 150 pixels of the previously determined elevation were fit using a high-order polynomial. Our refined estimate of the interface height was based on the vertical location corresponding to the maximum of the derivative of the polynomial. Thus we could measure the variation of the gravity current or first front interface height

with y or, by averaging over all 18 bands, compute the mean elevation over the width of the entire right-hand side of the tank.

A list of the experiments performed is shown in Appendix B, table 1. We regard the bead diameter, d_0, and the plume source volume flux, Q_0, and reduced gravity, g'_0, as independent variables. From these, the following derived variables were computed: the source buoyancy flux, F_0, Reynolds number, Re_0, Péclet number, Pe_0, and the permeability of the porous medium, k. Note that $F_0 = Q_0 g'_0$. Moreover, Re_0 is given by $\mathrm{Re}_0 = Q_0 d_0/(A_{\mathrm{nozzle}}\nu)$. In the majority of experiments, the source Reynolds number was $\mathrm{Re}_0 \approx \mathcal{O}(10)$. (Note that Re_0 is the maximum value of the Reynolds number, which decreases with increasing x as $\mathrm{Re} \propto (x+x_0)^{-1/4}$). In all cases, the source Péclet number, $\mathrm{Pe}_0 = Q_0 d_0 \tau/(A_{\mathrm{nozzle}} D_d) > 100$, where the molecular diffusion coefficient of the solute, D_d, was estimated using the method suggested by Tyn and Calus – see (11-9.5) of Poling *et al.* (2000) and following Winsauer *et al.* (1952) the tortuosity constant was assumed to be $\tau = 2.0$ for $\phi = 0.38$. Furthermore, the permeability of the porous medium, corresponding to a medium comprised of uniform spherical beads, is calculated based on the empirical relationship derived originally by Rumpf and Gupte, and subsequently applied by Acton *et al.* (2001), Lyle *et al.* (2005) and many others, such that $k = \dfrac{{d_0}^2 \phi^{5.5}}{5.6}$.

4. Results and discussion

Illustrative experimental images are shown in figure 6. The curves on top of the laboratory images show the measured heights of the gravity current and first fronts. Panel a shows the time instant $t = 0$ at which the descending plume, dyed purple, first reaches the impermeable bottom boundary. Thereafter, a rightward propagating gravity current is formed, as exhibited in panel b. Although our equations of section 2.2 assume a gravity current of a constant reduced gravity and corresponding gravity current density, we see

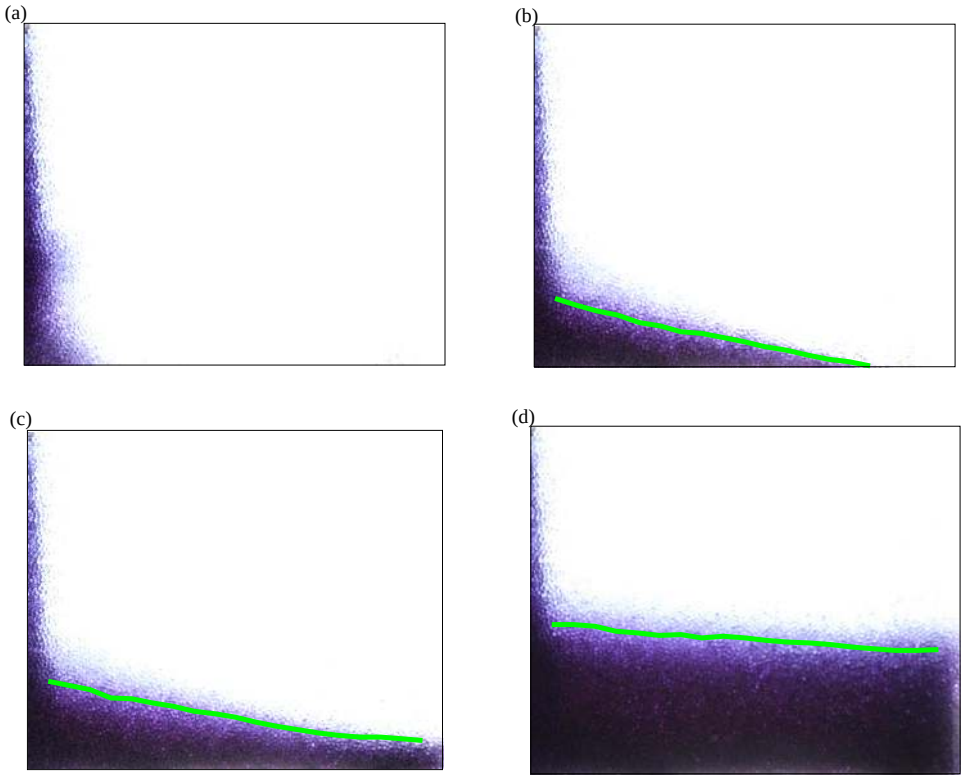

Figure 6: [Colour online] Plume, gravity current and curved interface experimental images. Images correspond to Experiment 13 at (a) $t = 0$, (b) $t = 0.7t_L$, (c) $t = t_L + 0.1t_H$ and (d) $t = t_L + 0.3t_H$ where t_L and t_H are defined by (2.34) and (2.43), respectively. The curves shown in (b), (c) and (d) are the interface heights as computed using the Matlab algorithm of section 3. The field of view for each image measures 44 cm long $\times$ 36 cm tall.

in this experimental image evidence of a horizontal density gradient within the gravity current. By combining Darcy's law, a hydrostatic pressure equation and Leibniz's rule, it can be shown that this density gradient is dynamically insignificant provided

$$\left|(\rho - \rho_0)\frac{\partial h}{\partial y}\right| \gg \left|\int_0^h \frac{\partial \rho}{\partial y}\,\mathrm{d}(H-h)\right|.$$

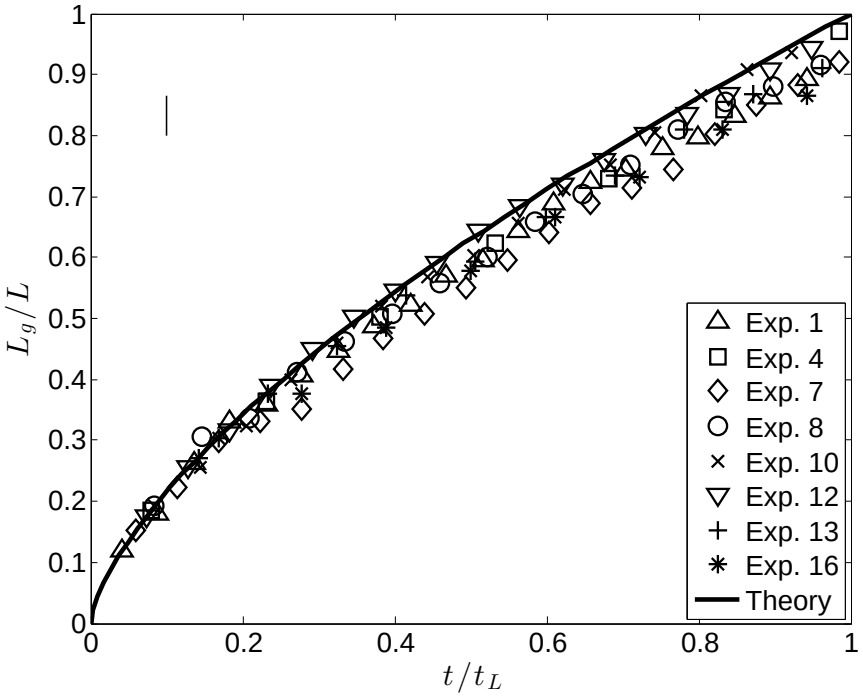

Figure 7: Gravity current front position vs. time. A representative error bar is indicated in the upper left hand side corner.

We assume that $\rho \propto I$, where I is the intensity of the false-colour grayscale laboratory images and note that $I(\rho = \rho_0) = 0$. Therefore the condition to be satisfied becomes:

$$\left| I \frac{\partial h}{\partial y} \right| \gg \left| \int_0^h \frac{\partial I}{\partial y} \, \mathrm{d}(H - h) \right|.$$

A separate analysis, not presented here, confirms that the above inequality is satisfied in our experiments. Thus we conclude that the assumption made in deriving (2.26) is appropriate. Finally, panels c and d correspond to times greater than t_L. Discharged plume fluid accumulates in a deepening layer of contaminated fluid at the bottom of the control volume. Qualitatively, the shapes of the gravity current and of the first front are similar to the results displayed in figures 3 and 4, respectively. However, to make this comparison between the analytical predictions of section 2 and the experimental

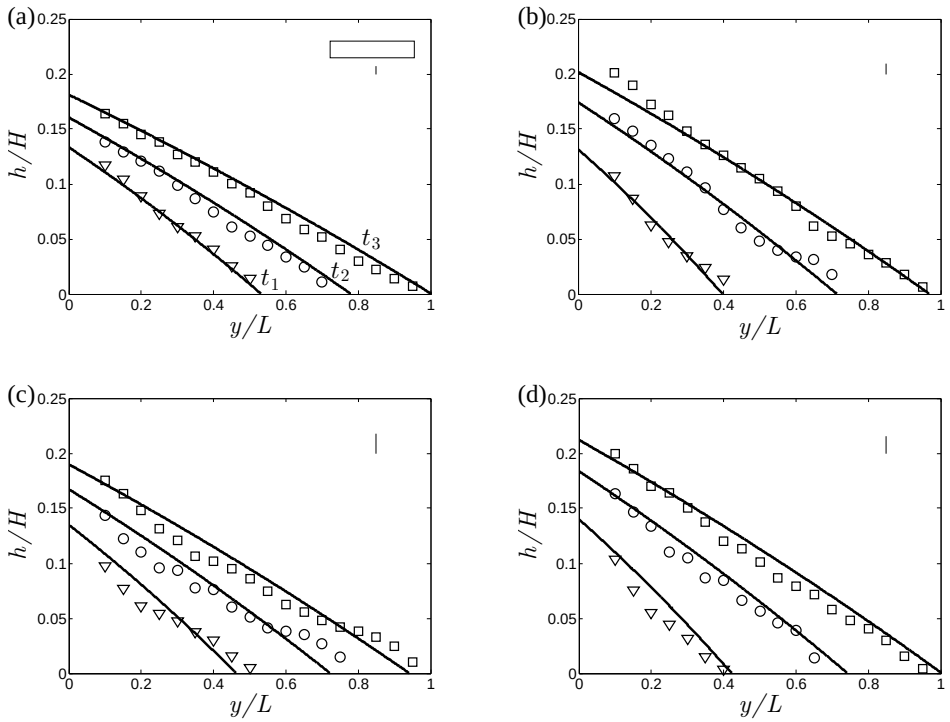

Figure 8: Gravity current profile: (a) Experiment 1, $t_1 = 0.37t_L$, $t_2 = 0.67t_L$, $t_3 = 1.0t_L$, (b) Experiment 4, $t_1 = 0.25t_L$, $t_2 = 0.60t_L$, $t_3 = 0.95t_L$, (c) Experiment 10, $t_1 = 0.34t_L$, $t_2 = 0.64t_L$, $t_3 = 0.95t_L$, and (d) Experiment 13, $t_1 = 0.27t_L$, $t_2 = 0.64t_L$, $t_3 = 1.0t_L$. The time scales t_L and t_H are defined by (2.34) and (2.43), respectively. Representative average error bars are indicated in the upper right hand side corner of each figure. Also, a rectangle having unit aspect ratio in physical coordinates is indicated in panel a.

measurements of section 3 quantitatively meaningful, it is first necessary to estimate the numerical value of α, which first appears in (2.8) and reappears, for instance, in (2.22) and (2.42). For this purpose, we focus specifically on the long time measurements of the first front elevation. (Note that, following the studies of free turbulent plumes e.g. Baines & Turner 1969, measuring the elevation of the first front is much more straightforward than trying to directly determine the plume volume flux and its variation with x). Using

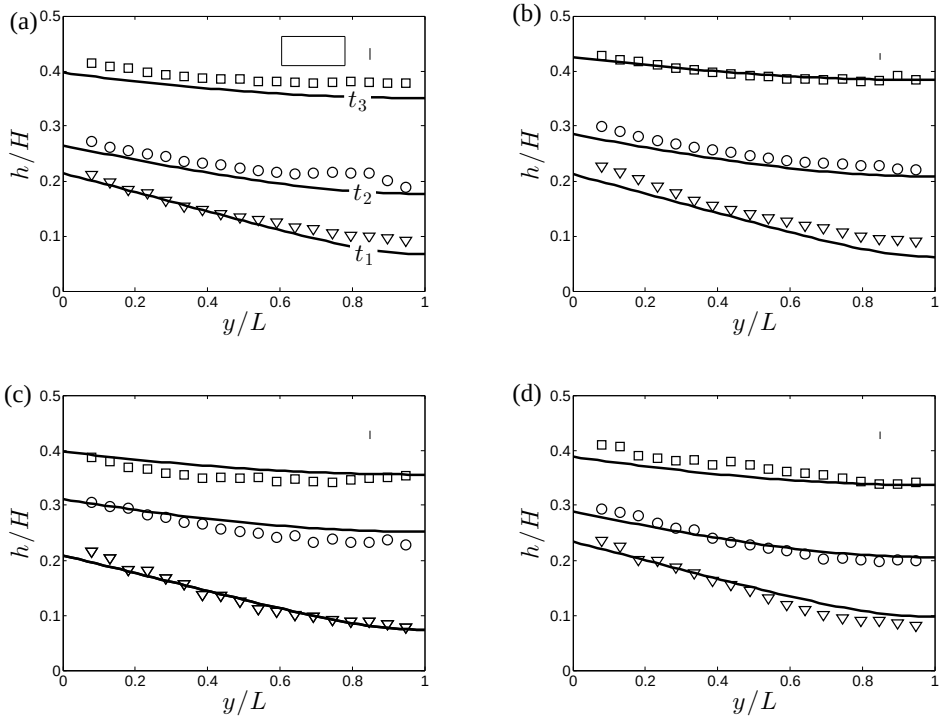

Figure 9: Curved interface profile: (a) Experiment 1, $t_1 = t_L + 0.04t_H$, $t_2 = t_L + 0.08t_H$, $t_3 = t_L + 0.13t_H$, (b) Experiment 4, $t_1 = t_L + 0.04t_H$, $t_2 = t_L + 0.08t_H$, $t_3 = t_L + 0.13t_H$, (c) Experiment 10, $t_1 = t_L + 0.03t_H$, $t_2 = t_L + 0.09t_H$, $t_3 = t_L + 0.14t_H$, and (d) Experiment 13, $t_1 = t_L + 0.04t_H$, $t_2 = t_L + 0.07t_H$, $t_3 = t_L + 0.11t_H$. The time scales t_L and t_H are defined by (2.34) and (2.43), respectively. Representative average error bars are indicated in the upper right hand side corner of each figure and a rectangle having unit aspect ratio in physical coordinates is indicated in panel a.

(2.40) as the reference analytical solution, the error-minimizing value of α is determined for each experiment. We then compute the average over all 16 experiments from table 1 of Appendix B and find a mean value of $\alpha = 0.015$ cm. The mean errors presented in table 1 have standard and maximum deviations of $\pm 3\%$ and $\pm 5\%$ for the entire data set.

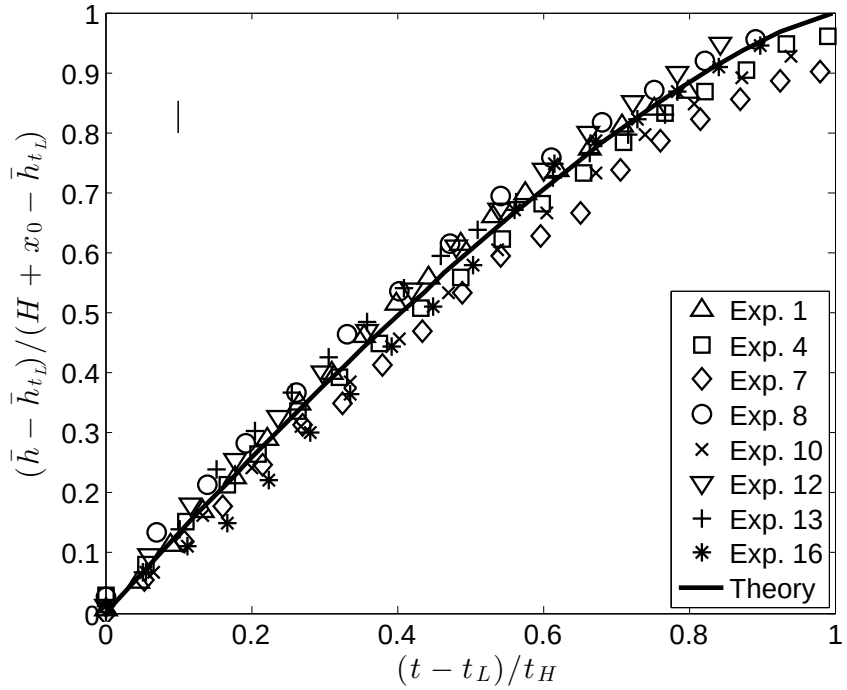

Figure 10: First front elevation vs time. A representative error bar is indicated in the upper left hand side corner.

The small values just reported support the hypothesis that $\alpha = 0.015$ cm is a meaningful average value.

With this value for α to hand, separate comparisons can be made for the gravity current and first front problems. Starting with the gravity current, two different comparisons between theory and experiment are drawn: (i) the front position vs. time, t (figure 7), and (ii) the gravity current profile for various times (figure 8). In figure 7, the solid curve is adopted from (2.35). For clarity, we do not include the entirety of our experimental data set but rather choose eight representative experiments from table 1 that span small and large Q_0, g_0' and d_0. Because the plume has a finite thickness when it reaches the bottom of the control volume at $t = 0$ (see figure 6 a), the initial gravity current length is some finite value. Therefore measured values for $L_g > 0$ when $t = 0$. To make a

consistent comparison with the predictions of (2.35) for which $L_g = 0$ when $t = 0$, it is therefore necessary to adjust the measured data so that the first data point of each set coincides with the solid curve. The meaningful comparison to be drawn between theory and experiment is therefore for intermediate and large values of t; in the former case, good agreement is observed whereas in the latter case predicted values for L_g typically over-predict their measured counterparts. This observation is consistent with Huppert & Woods (1995), who, in their investigation of a constant volume release in a Hele-Shaw cell, made similar observations and attributed their discrepancy to the influence of bottom friction near the front (see e.g. their figures 2 and 3). In figure 8, we show the gravity current profile at three distinct times for four different experiments. Experiments are chosen on the basis of their values for F_0 and d_0, being in some instances comparatively small and in others comparatively large. In all cases, the measured heights show good agreement with the profiles predicted from (2.30). The positive comparisons drawn in figures 7 and 8 constitute an indirect validation for the computed value of α: the influx to the gravity current depends on Q_g and g'_g, which are, in turn, functions of α as prescribed, for instance, by (2.22) and (2.23).

In considering the first front, figure 9 compares the measured and predicted first front elevations for the same experiments, 1, 4, 10 and 13, as are considered in figure 7. In all cases, and consistent with figure 4, it is observed that the first front becomes more horizontal as t increases. Equation (2.38) shows that the elevation, h, of the first front depends upon the total volume, V, of plume fluid discharged into the lower layer up until that particular instant in time. Hence the minor discrepancies observed in figure 9 are likely the result of differences in the values of the actual volume flux vs. that estimated from (2.22).

Furthermore, we can estimate the y-averaged first front elevation vs. time by adopting

(2.42). Results are shown in figure 10, which includes the same set of representative experiments as in figure 7. We do not separately show the solution of (A 1) because this curve overlaps with the solid curve already present in figure 10. Elevations are non-dimensionalized by $H + x_0 - \bar{h}_{t_L}$ where x_0 is defined by (2.21) and $\bar{h}_{t_L}$ is defined by (2.36). Conversely, the abscissa is non-dimensionalized by t_H, which is defined by (2.43). The overall comparison between theory and experiment is favourable. In particular, both suggest that the speed of ascent decreases as the first front approaches the source. This behaviour is qualitatively consistent with (2.22) and (2.41), the former of which indicates that the plume volume flux scales as $x^{1/4}$.

We tried rationalizing the variation of the (non-dimensionalized) data by grouping our experimental measurements into different families according to the values of g_0', Q_0 or d_0. For better or worse, this analysis did not reveal any definitive trends other than that the first front elevation is moderately larger for small Q_0 – see figure 10. On this basis, we conclude that the non-dimensionalizations outlined above are appropriate in that they capture the leading order physics of the flow.

A video comparing the numerical and experimental height profiles of the gravity current and first front for Experiment 13 is included as Electronic Supplementary Material (Movie.mp4). The video is made in Matlab by first combining 29 images, spaced at 20 s intervals where the horizontal and vertical axes are respectively normalized by L and H. Analogue numerical solutions are then superposed on top of the experimental images where we use the equations of sections 2.2 and 2.3, respectively, when $t < t_L$ and $t > t_L$.

5. Conclusions

Motivated by studies of filling box flows with turbulent free plumes (Baines & Turner 1969), and based on previous investigations of laminar plumes (Wooding 1963; Roes *et al.*

2014) and gravity current flow (Huppert & Woods 1995) in porous media, a solution for filling box flows in the Darcy regime with Pe $\gg \mathcal{O}(1)$ is derived. We assume a Boussinesq system where the dense and light fluids are fully miscible. The following three flow components are considered: (i) a (negatively-buoyant) laminar plume, (ii) a pair of gravity currents comprised of discharged plume fluid that propagate along the bottom of the control volume and (iii) the subsequent vertical advection of the discharged plume fluid towards the source.

In section 2.1, we derive a similarity solution for laminar plume flow. This solution assumes that molecular diffusion is negligible compared to mechanical dispersion, D, and so applies in the "inner" region close to the plume axis where flow speeds are comparatively large. In the context of (1.1), we assume that Pe $\gg \mathcal{O}(1)$. The solution is derived by employing a tranverse dispersivity constant, α, in the governing equation (2.11) whose value, 0.015 cm, is determined by comparison with experimental measurements. In the inner region, variables such as the fluid density and vertical velocity change rapidly in the horizontal direction, y, so that a Wooding-type boundary-layer approximation can be applied in deriving the self-similar solution. In the outer region, by contrast, we assume that the vertical velocity and density perturbation are both zero. Our solution is therefore qualitatively similar to the "top hat" description of turbulent free plumes, first proposed by Morton *et al.* (1956), where molecular diffusion is likewise ignored.

The self-similar solution allows us to compute the plume volume flux, Q, and mean reduced gravity, $\bar{g}'$, as functions of x, the vertical coordinate. Indeed (2.22) and (2.23) respectively indicate that Q and $\bar{g}'$ are proportional to $x^{1/4}$ and $x^{-1/4}$ contrary to the scalings $x^{1/3}$ and $x^{-1/3}$ that apply when Pe $\lesssim \mathcal{O}(1)$ (Wooding 1963; Roes *et al.* 2014). The values of Q and $\bar{g}'$ calculated at the bottom of the control volume, comprise the source conditions for the pair of gravity currents that are formed when the plume encounters

the impermeable bottom boundary. The equations governing porous media gravity current flow are reviewed in section 2.2. In particular, the self-similar ODE (2.31), originally derived by Huppert & Woods (1995) for (hydrostatic) gravity current flow and based on Darcy's law (2.26) and a volume conservation equation (2.27), describes the variation of the gravity current height in space and time. The self-similar ODE (2.31), and associated boundary conditions (2.32), is solved by employing a shooting method to draw curves such as those shown in figure 3. Once the gravity current reaches the (impermeable) vertical sidewall of the control volume at $t = t_L$, the motion becomes primarily vertical. The solution describing the motion of the first front, the interface separating the discharged plume fluid from the overlying ambient fluid, is presented in section 2.3. Similar to the gravity current problem, the equation that describes the spatio-temporal evolution of the first front, (2.39), is also based on Darcy's law and a volume conservation equation. However, in this case no self-similar solution is possible and hence a finite difference numerical method is applied instead. Figure 4 indicates that the first front, whose initial shape matches that of the gravity current at $t = t_L$, becomes progressively more horizontal with time so that, in the large t limit, the first front moves only vertically. Moreover, the advection speed of the first front decreases as it moves towards the plume source.

To verify key model predictions, complementary experiments are performed using fresh water and salt water as the working fluids. Particular emphasis is placed on the motion of the gravity current and of the first front, both of which depend on Q and $\bar{g}'$. A comparison between theory and experiment is given in section 4. Figures 7 and 8 show, respectively, the gravity current front position, L_g, vs. t, and the gravity current height, h, vs. y at three different instants in time. Conversely figure 9 shows the shape of the first front, again for three different values of t. Finally figure 10 presents the time variation of the average first front elevation, $\bar{h}$. In all cases, the agreement between the predictions and

the measurements is promising. Thus, the experimental measurements provide support for the functional form of our plume solution according to which $Q \propto x^{1/4}$.

By necessity, the present research is conducted using a set of limiting assumptions: the medium is isotropic, the fluids are miscible and the flow is both Boussinesq and of Darcy type. In many geological scenarios of interest, however, other factors e.g. surface tension and anisotropy may be relevant. In future research, the most restrictive of our assumptions will be relaxed by studying filling box flow in media characterized by spatially-variable ϕ and k. Further extensions of the research could include an examination of non-Boussinesq and/or non-Darcy flow.

Acknowledgments

The current research is supported by NSERC (Discovery Grant and RTI programmes) and Carbon Management Canada. The authors acknowledge the kind assistance provided by Mark Roes in setting up the experiment and in writing the image post-processing algorithms used in extracting the data shown in figures 8, 9 and 10. The authors also wish to thank Swapnil Dalal for fruitful discussions concerning the numerical schemes described in section 2.3. Experiments were conducted in the laboratory of Dr. Bruce R. Sutherland.

Appendix A. Curved interface methodology

In this appendix, we present the details of the numerical technique employed to solve for the motion of the (curved) first front.

Space and time derivatives are discretized so that (2.39) is replaced by

$$\frac{h_i^{n+1} - h_i^n}{\Delta t} = \frac{S}{2\Delta y^2}(h_{i-1}^{n+1}h_{i-1}^n - 2h_i^{n+1}h_i^n + h_{i+1}^{n+1}h_{i+1}^n) \tag{A 1}$$

where i and n represent space and time indices, respectively. By symmetry, we only

concern ourselves with the right-hand side of the control volume so that $i = 1$ corresponds to the box centerline at $y = 0$ whereas $i = L/\Delta y + 1 = I + 1$ corresponds to the position of the right sidewall at $y = L$. On further simplification and rearranging, (A 1) becomes,

$$-(Rh_{i-1}^n)h_{i-1}^{n+1} + (1 + 2Rh_i^n)h_i^{n+1} - (Rh_{i+1}^n)h_{i+1}^{n+1} = h_i^n \tag{A 2}$$

where $R = \dfrac{S\Delta t}{2\Delta y^2}$. In matrix form, (A 2) is expressed as

$$\begin{bmatrix} 1+2Rh_2^n & -Rh_3^n & 0 & 0 & \dots & 0 \\ -Rh_2^n & 1+2Rh_3^n & -Rh_4^n & 0 & \dots & 0 \\ & & & \ddots & & \\ 0 & \dots & 0 & -Rh_{I-1}^n & 1+2Rh_I^n & -Rh_{I+1}^n \\ 0 & \dots & 0 & 0 & -2Rh_I^n & 1+2Rh_{I+1}^n \end{bmatrix} \begin{bmatrix} h_2^{n+1} \\ h_3^{n+1} \\ h_4^{n+1} \\ \vdots \\ h_{I-1}^{n+1} \\ h_I^{n+1} \\ h_{I+1}^{n+1} \end{bmatrix} = \begin{bmatrix} h_2^n + Rh_1^n h_1^{n+1} \\ h_3^n \\ h_4^n \\ \vdots \\ h_{I-1}^n \\ h_I^n \\ h_{I+1}^n \end{bmatrix} \tag{A 3}$$

The additional factor of 2 that appears in matrix entry $(I, I-1)$ is due to the application of a "ghost point" (Causon & Mingham 2010), which is required because of the no-flux boundary condition at the sidewalls i.e. $\partial h/\partial y = 0$ when $y = \pm L$.

Equation (A 3) is solved using a shooting method. Thus an initial guess is provided for h_1^{n+1}, whose value is refined through iteration whilst enforcing volume conservation via (2.38) (Causon & Mingham 2010). The discrete form of (2.38) reads

$$\phi\Delta y \sum_{i=1}^{I} \left[\frac{(h_{i+1}^{n+1} + h_i^{n+1})}{2} - \frac{(h_{i+1}^n + h_i^n)}{2} \right] = Q_g(H - h_1^n)\Delta t. \tag{A 4}$$

The left hand side of (A 4), discretized in space, represents the volume displaced by the advancing first front over time Δt, whereas the right hand side of the equation, discretized in time, represents the volume of discharged plume fluid supplied over the same time interval.

Appendix B. Experimental details

Table 1 provides the details of the experiments described in section 3. Parameters such as F_0, Re_0 and Pe_0 are defined previously whereas Re_H, the plume Reynolds number at the bottom of the control volume is estimated from

$$\mathrm{Re}_H = \frac{U(H)d_0}{\nu} = \left[\left(\frac{4F_0k}{\pi^3\nu^3\Lambda}\right)^2 \frac{\alpha^3}{\phi(H+x_0)}\right]^{1/4}. \tag{B 1}$$

The velocity $U(x) = \dfrac{\alpha u(x)}{d_0}$ is a characteristic velocity where the transport velocity $u(x)$ is calculated by dividing the plume volume flux by its cross-sectional area. Thus,

$$U(x) = \frac{\alpha}{d_0}\frac{Q(x)}{\Lambda[y(\eta=\pi) - y(\eta=-\pi)]}. \tag{B 2}$$

Finally the error, ϵ, is calculated via

$$\epsilon = \frac{100\%}{N}\left(\sum_1^N \frac{\bar{h}_{ex} - \bar{h}_{th}}{\bar{h}_{ex}}\right), \tag{B 3}$$

where N is the number of experimental images collected (typically 60) and $\bar{h}_{ex}$ and $\bar{h}_{th}$ are the time-dependent measured and predicted first front heights. The value of $\bar{h}_{th}$, determined from (2.42), directly depends upon the plume volume flux, Q. Therefore, it is understood that the value of ϵ obtained using (B 3) incorporates the deviation of the theoretically predicted volume flux from its corresponding experimental value.

REFERENCES

Acton, J. M., Huppert, H. E. & Worster, M. G. 2001 Two-dimensional viscous gravity currents flowing over a deep porous medium. *J. Fluid Mech.* **440**, 359–380.

Baines, S. J. & Worden, R. H. 2004 Geological storage of carbon dioxide. *Geological Society, London* **233**, 1–6.

Baines, W. D. & Turner, J. S. 1969 Turbulent buoyant convection from a source in a confined region. *J. Fluid Mech.* **37**, 51–80.

Bear, J. 1972 *Dynamics of fluids in porous medium*. American Elsevier.

Exp#	d_0 (cm)	k ($\frac{\text{cm}^2}{10000}$)	Q_0 ($\frac{\text{cm}^3}{\text{s}}$)	g_0' ($\frac{\text{cm}}{\text{s}^2}$)	F_0 ($\frac{\text{cm}^4}{\text{s}^3}$)	Re_0	Re_H	Pe_0 ($\times 10^3$)	ϵ (%)
1	0.3	0.78	0.20	24.53	4.91	2.14	0.05	1.60	1.65
2	0.3	0.78	0.49	24.53	12.02	5.25	0.08	3.92	4.72
3	0.3	0.78	0.75	24.53	18.39	8.04	0.10	6.00	3.25
4	0.3	0.78	0.90	54.94	49.44	9.64	0.17	7.20	-2.29
5	0.3	0.78	0.18	54.94	9.89	1.93	0.08	1.44	0.21
6	0.3	0.78	0.84	54.94	46.15	9.00	0.17	6.72	1.93
7	0.3	0.78	0.17	85.35	14.51	1.82	0.09	1.36	-3.49
8	0.3	0.78	0.90	85.35	76.81	9.64	0.22	7.20	1.58
9	0.3	0.78	0.53	85.35	45.23	5.68	0.17	4.24	1.98
10	0.5	2.20	0.30	21.09	6.33	5.36	0.10	4.00	-4.27
11	0.5	2.20	0.60	21.09	12.65	10.71	0.15	8.00	-4.85
12	0.5	2.20	1.00	21.09	21.09	17.86	0.19	13.3	-3.48
13	0.5	2.20	1.00	58.86	58.86	17.86	0.32	13.3	1.37
14	0.5	2.20	0.60	58.86	35.32	10.71	0.25	8.00	-4.38
15	0.5	2.20	0.61	94.18	57.45	10.89	0.32	8.13	-4.85
16	0.5	2.20	0.92	94.18	86.64	16.43	0.39	12.26	-3.72

Table 1: A summary of the experimental parameters: bead diameter, d_0, permeability, k, source volume flux, Q_0, source reduced gravity, g_0', source buoyancy flux, F_0, source Reynolds number, Re_0, plume Reynolds number at the bottom boundary, Re_H (defined in B 1), source Péclet number, Pe_0, and the mean error, ϵ (defined in B 3).

Bear, J. & Verruijt, A. 1987 *Modelling Groundwater Flow and Pollution*. D. Reid, Norwell, MA, USA.

Bickle, M., Chadwick, A., Huppert, H. E., Hallworth, M. & Lyle, S. 2007 Modelling carbon dioxide accumulation at Sleipner: Implications for underground carbon storage. *Earth and Planetary Science Letters* **255**, 164–176.

Britter, B. E. 1979 The spread of a negatively buoyant plume in a calm environment. *Atmospheric Environment* **13**, 1241–1247.

Caulfield, C. P. & Woods, A. W. 2002 The mixing in a room by a localized finite-mass-flux source of buoyancy. *J. Fluid Mech.* **471**, 33–50.

Causon, D.M. & Mingham, C. G. 2010 *Introductory Finite Difference Methods for PDEs*. Ventus Publishing ApS.

Chen, K. S. & Ho, J. R. 1986 Effect of flow inertia on vertical natural convection in saturated porous media. *Int. J. Heat Mass Transfer* **29**, 753–759.

Delgado, J. M. P. Q. 2007 Longitudinal and transverse dispersion in porous media. *IChemE* **85 (A9)**, 1245–1252.

Dullien, F. A. L. 1992 *Porous medium fluid transport and pore structures*. Academic press.

Ennis-King, J. & Paterson, L. 2003 Role of convective mixing in the long-term storage of carbon dioxide in deep saline formations. *Society of Petroleum Engineers Inc.* **SPE 84344**,1–12.

Germeles, A. E. 1975 Forced plumes and mixing of liquids in tanks. *J. Fluid Mech.* **71**, 601–623.

Happel, J. & Brenner, H. 1991 *Low Reynolds Number Hydrodynamics: With Special Applications to Particulate Media*, 2nd edn. Kluwer Academic.

Houseworth, J. E. 1984 Longitudinal dispersion in non-uniform, isotropic porous media. *Tech. Rep.* KH-R-45. California Institue Of Technology, Pasadena, California.

Hughes, G. O. & Griffiths, R. W. 2006 A simple convective model of the global overturning circulation, including effects of entrainment into sinking regions. *Ocean Modelling* **12**, 46–79.

Hunt, G. R. & Kaye, N. G. 2001 Virtual origin correction for lazy turbulent plumes. *J. Fluid Mech.* **435**, 377–396.

Huppert, H. E. & Woods, A. W. 1995 Gravity-driven flows in porous layers. *J. Fluid Mech.* **292**, 55–69.

Kaye, N. B. & Hunt, G. R. 2007 Overturning in a filling box. *J. Fluid Mech.* **576**, 297–323.

Khachikian, C. & Harmon, T. C. 2000 Nonaqueous phase liquid dissolution in porous media: current state of knowledge and research needs. *Transport in Porous Media* **38**, 3–28.

Kueper, B. H., Wealthall, G. P., Smith, J. W. N., Leharne, S. A. & Lerner, D. N. 2003 An illustrated handbook of dnapl transport and fate in the subsurface. *Tech. Rep.* R&D Publication 133. Environment Agency.

Lai, F. C. 1991 Non-darcy convection from a line source of heat in a saturated porous medium. *Int. Comm. Heat Mass Transfer* **18**, 445–457.

Linden, P. F., Lane-Serff, G. F. & Smeed, D. A. 1990 Emptying filling boxes: the fluid mechanics of natural ventilation. *J. Fluid Mech.* **212**, 309–335.

Lyle, S., Huppert, H. E., Hallworth, M., Bickle, M. & Chadwick, A. 2005 Axisymmetric gravity currents in a porous medium. *J. Fluid Mech.* **543**, 293–302.

MacMinn, C. W., Neufeld, J. A., Hesse M. A. & Huppert, H. E. 2012 Spreading and convective dissolution of carbon dioxide in vertically confined, horizontal aquifers. *Water Resources Research* **48, W11516**, 1–11.

Manins, P. C. 1979 Turbulent buoyant convection from a source in a confined region. *J. Fluid Mech.* **91**, 765–781.

Morton, B. R., Taylor, G. I. & Turner, J. S. 1956 Turbulent gravitational convection from maintained and instantaneous sources. *Proc. R. Soc. Lond.* **A 234**, 1–23.

Nabi, S. & Flynn, M. R. 2013 The hydraulics of exchange flow between adjacent confined building zones. *Building and Environment* **59**, 76–90.

Neufeld, J. A., Hesse, M. A., Riaz, A., Hallworth, M. A., Tchelepi, M. A. & Huppert, H. E. 2010 Convective dissolution of carbon dioxide in saline aquifers. *Geophysical Research Letters* **37, L22404**, 1–5.

Nield, D. A. & Kuznetsov, A. V. 2013 An historical and topical note on convection in porous media. *Journal of Heat Transfer* **135, 061201**, 1–10.

Poling, B. E., Prausnitz, J. M. & O'Connell, J. P. 2000 *The Properties of Gases and Liquids*. McGraw-Hill.

Roes, M. A. 2014 Buoyancy-driven convection in a ventilated porous medium. Master's thesis, University of Alberta.

Roes, M. A., Bolster, D. T. & Flynn, M. R. 2014 Buoyant convection from a discrete source in a leaky porous medium. *J. Fluid Mech.* **755**, 204–229.

Winsauer, W. O. and Shearin, H. M. and Masson, P. H. and Williams, M. 1952 Resistivity of brine-saturated sands in relation to pore geometry. *AAPG Bull.* **36–2**, 253–277.

Wooding, R. A. 1963 Convection in a saturated porous medium at large Rayleigh number or Péclet number. *J. Fluid Mech.* **15**, 527–544.